PHOTONICS Research

Generating superposed terahertz perfect vortices via a spin-multiplexed all-dielectric metasurface

FAN HUANG,[1] QUAN XU,[1,4] (ORCID) WANYING LIU,[1] TONG WU,[1] JIANQIANG GU,[1,5] JIAGUANG HAN,[1,2] AND WEILI ZHANG[3]

[1]*Center for Terahertz Waves and College of Precision Instrument and Optoelectronics Engineering, Tianjin University and Key Laboratory of Optoelectronics Information and Technology (Ministry of Education), Tianjin 300072, China*
[2]*Guangxi Key Laboratory of Optoelectronic Information Processing, School of Optoelectronic Engineering, Guilin University of Electronic Technology, Guilin 541004, China*
[3]*School of Electrical and Computer Engineering, Oklahoma State University, Stillwater, Oklahoma 74078, USA*
[4]*e-mail: quanxu@tju.edu.cn*
[5]*e-mail: gjq@tju.edu.cn*

Perfect optical vortices (POVs), characterized as a ring radius independent of topological charge (TC), possess extensive application in particle manipulation and optical communication. At present, the complex and bulky optical device for generating POVs has been miniaturized by leveraging the metasurface, and either spin-dependent or spin-independent POV conversions have been further accomplished. Nevertheless, it is still challenging to generate superposed POVs for incidences with orthogonal circular polarization. Here, a spin-multiplexed all-dielectric metasurface method for generating superposed POVs in the terahertz frequency range is proposed and demonstrated. By using the multiple meta-atom comprised structure as the basic unit, the complex amplitude of two superposed POVs is modulated, decoupled, and subsequently encoded to left- and right-handed circular polarization incidences. Furthermore, two kinds of metasurfaces are fabricated and characterized to validate this controlling method. It is demonstrated that the measured intensity and phase distributions match well with the calculation of the Rayleigh–Sommerfeld diffraction integral, and the radius of superposed POVs is independent of TCs. This work provides promising opportunities for developing ultracompact terahertz functional devices applied to complex structured light generation and terahertz communication, and exploring sophisticated spin angular momentum and orbital angular momentum interactions like the photonic spin-Hall effect.   © 2023 Chinese Laser Press

https://doi.org/10.1364/PRJ.476120

1. INTRODUCTION

Phase and polarization are two nontrivial characteristics of light [1]. Circularly polarized light owns spin angular momentum (SAM) of $\sigma\hbar$ per photon attributed to the orthogonal handedness [2], where $\sigma = \pm 1$ represents the spin of left- and right-handed circular polarization (LCP and RCP). On the other hand, orbital angular momentum (OAM) is expressed as $l\hbar$, where l is the topological charge (TC)—an integer of single quantum number [3]. The beam that carries OAM, named the optical vortex beam (OVB), has an undefined phase in the center of its helical phase structure, which is described by an azimuthal phase dependence $\exp(il\theta))$ and enables the intensity distribution to be like a doughnut [4]. The whole angular momentum of a circularly polarized OVB can be expressed by $J = (\sigma + l)\hbar$ per photon, including both SAM and OAM [5,6]. Over the past 30 years, OVB has been explored in depth

and has led to a number of applications in fields such as particle manipulation, high-resolution microscopy, optical communication, and quantum information [7–11], while traditional OVB generation methods including diffractive optical elements [12], spiral phase plates [13], and spatial light modulators are either bulky or inflexible, hindering the further development of this field.

Recently, the metasurface has emerged as a compact approach for OVB generation through the design of suitable subwavelength meta-atoms and the arrangement of their spatial distributions [14–21]. In particular, the implantation of the geometric phase endows arbitrary and dispersionless phase engineering for circular polarization by simply tuning the orientation angle, providing great flexibilities for the SAM-to-OAM conversion of light [22–25]. Further in conjunction with spin-independent design methods, such as the propagation phase, arbitrary optical SAM-to-OAM conversion can be achieved,

that is, independent OVB generation under LCP and RCP incidences [26]. Notably, the beam radii of these conventional OVBs always depend on their TC number, limiting their application in some scenarios, for example, coupling multiple OVBs into an optical component with a fixed annular profile for mode division multiplexing. In order to overcome this limitation, the concept of perfect optical vortices (POVs) has been proposed, whose beam radii are independent of the TCs [27–32]. So far, in the reports of metasurface-based POV generation, both spin-dependent and spin-independent [33–37], only a single POV can be generated under LCP or RCP incidence, corresponding to a one-to-one SAM-to-OAM conversion.

In this paper, a metasurface-based method for spin-distinguished generation of superposed POVs is proposed. This is achieved by adopting the multiple meta-atoms comprised structure, namely, the meta-molecule as the basic unit to independently manipulate the output phases and amplitudes of orthogonal circular polarizations [21]. In this manner, the designed metasurface can totally tailor and decouple the complex amplitude of two superposed POVs, subsequently imposing the corresponding information to the orthogonal circular polarization. Based on this meta-molecule, we have designed and testified two metasurface samples (Metasurface-I and Metasurface-II) in the terahertz domain and found the measured intensity and phase distribution are well matched with the calculation of the Rayleigh–Sommerfeld diffraction integral. The proposed design strategy opens an avenue toward the ultracompact terahertz functional devices and sophisticated SAM–OAM interaction, which may find applications in terahertz communication, producing complex structured light and exploring photonic spin-Hall effect.

2. RESULTS AND DISCUSSION

A. Design Principle

The envisioned function of the metasurface is to independently convert orthogonal circular polarization to superposed POVs, and these unique responses are illustrated in Fig. 1. The POV can be generated by Fourier transform of the Bessel–Gaussian beam, in which the Bessel–Gaussian beam can be generated by an axicon and the Fourier transform operation can be achieved by a spherical lens. The overall phase profile of a POV, provided by the designed metasurface, has a form of

$$\varphi(x,y) = -2\pi \frac{\sqrt{x^2+y^2}}{d} + l \times \arctan\left(\frac{x}{y}\right) + \frac{2\pi}{\lambda}$$
$$\times \left(f - \sqrt{x^2+y^2+f^2}\right), \quad (1)$$

where the first item represents the axicon's phase profile φ_{axicon}, in which d is the axicon period determining the ring radius of the POV. The second item corresponds to the spiral phase profile φ_{spiral} carrying the OAM with a TC of l. The last item is the phase profile of a spherical lens, in which f is its focal length and λ is the operating wavelength [38,39]. The phase profile of the spherical lens is very similar to that of a parabolic lens $\varphi = -\pi(x^2+y^2)/\lambda f$.

In conjunction with the above phase distribution of the POV, the ultimate complex amplitude formed by the superposition of two POVs can be calculated. When LCP is incident on
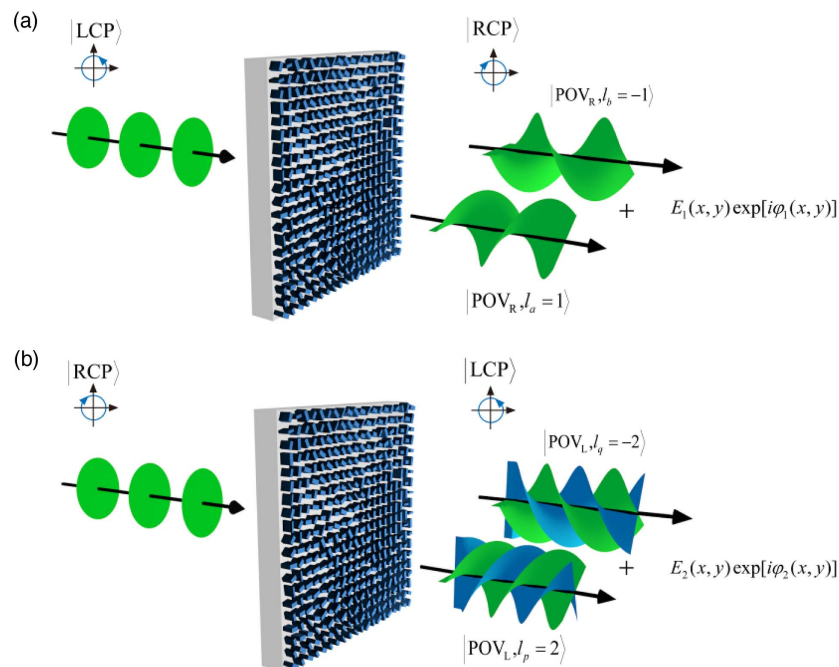
Fig. 1. Functional schematic of designed metasurface. (a) Phase and amplitude manipulation for LCP incidence. The generated multiplex amplitude $E_1(x,y)\exp[i\varphi_1(x,y)]$ is the superposition of POVs $|\text{POV}_L, l_a = 1\rangle$ and $|\text{POV}_L, l_b = -1\rangle$. (b) Phase and amplitude manipulation for RCP incidence. The generated multiplex amplitude $E_2(x,y)\exp[i\varphi_2(x,y)]$ is the superposition of POVs $|\text{POV}_R, l_p = 2\rangle$ and $|\text{POV}_R, l_q = -2\rangle$. For all the cases, only the flipped handedness to the incidence is considered in the output, and $E_1(x,y)\exp[i\varphi_1(x,y)]$ is independent of $E_2(x,y)\exp[i\varphi_2(x,y)]$.

the metasurface [Fig. 1(a)], the RCP output is expressed as a complex amplitude distribution $E_1(x,y) \exp[i\varphi_1(x,y)]$, which can be decomposed into two POVs $\exp[i\varphi_a(x,y)]$ with TC of l_a and $\exp[i\varphi_b(x,y)]$ with TC of l_b. Similarly, as the input is altered to RCP [Fig. 1(b)], the LCP output from the metasurface is $E_2(x,y) \exp[i\varphi_2(x,y)]$ comprising two POVs $\exp[i\varphi_p(x,y)]$ with a TC of l_p and $\exp[i\varphi_q(x,y)]$ with a TC of l_q. By adopting Jones vectors $|\text{LCP}\rangle = [1, i]^T$ and $|\text{RCP}\rangle = [1, -i]^T$ to represent the normal LCP and RCP incidences, respectively, the metasurface can be described by a Jones matrix $J(x,y)$ calculated as

$$\frac{1}{2}\begin{pmatrix} E_1(x,y)e^{i\varphi_1(x,y)} + E_2(x,y)e^{i\varphi_2(x,y)} & -i[E_1(x,y)e^{i\varphi_1(x,y)} - E_2(x,y)e^{i\varphi_2(x,y)}] \\ -i[E_1(x,y)e^{i\varphi_1(x,y)} - E_2(x,y)e^{i\varphi_2(x,y)}] & -[E_1(x,y)e^{i\varphi_1(x,y)} + E_2(x,y)e^{i\varphi_2(x,y)}] \end{pmatrix}. \tag{2}$$

Therefore, the transformations $J(x,y)|\text{LCP}\rangle = E_1(x,y) \exp[i\varphi_1(x,y)]|\text{RCP}\rangle$ and $J(x,y)|\text{RCP}\rangle = E_2(x,y) \cdot \exp[i\varphi_2(x,y)]|\text{LCP}\rangle$ are simultaneously satisfied, meaning the spin-distinguished superposed POV generation can be achieved. Despite $J(x,y)$ being a non-unitary matrix that cannot be directly diagonalized, we can transform $J(x,y)$ to $[J_M(x,y) + J_S(x,y)]/2$, where $J_M(x,y)$ and $J_S(x,y)$ are unitary and can be rewritten as $J_M(x,y) = R_M\Lambda_M R_M^{-1}$ and $J_S(x,y) = R_S\Lambda_S R_S^{-1}$, where Λ_M and Λ_S are the diagonal matrices, and the matrices R_M and R_S correspond to the rotation matrix for the Λ_M and Λ_S [Appendix D, Eqs. (D1) and (D2)]. This indicates that the metasurface includes two linear birefringent elements, in which the fast-axis orientation angle (θ) and the phase shift (δ_x and δ_y) of each element are ascertained by the eigenvector and eigenvalue of $J_M(x,y)$ and $J_S(x,y)$, respectively. For the given LCP and RCP inputs, $\delta_{M,x}$, $\delta_{M,y}$, and θ_M corresponding to $J_M(x,y)$ and $\delta_{S,x}$, $\delta_{S,y}$, and θ_S corresponding to $J_S(x,y)$ can be calculated as [Appendix D, Eqs. (D4) and (D5)] [21]

$$\begin{cases} \delta_{M,x} = [\varphi_1(x,y) + \varphi_2(x,y) + \arccos E_1(x,y) + \arccos E_2(x,y)]/2 \\ \delta_{M,y} = [\varphi_1(x,y) + \varphi_2(x,y) + \arccos E_1(x,y) + \arccos E_2(x,y)]/2 - \pi, \\ \theta_M = [\varphi_1(x,y) - \varphi_2(x,y) + \arccos E_1(x,y) - \arccos E_2(x,y)]/4 \end{cases} \tag{3}$$

$$\begin{cases} \delta_{S,x} = [\varphi_1(x,y) + \varphi_2(x,y) - \arccos E_1(x,y) - \arccos E_2(x,y)]/2 \\ \delta_{S,y} = [\varphi_1(x,y) + \varphi_2(x,y) - \arccos E_1(x,y) - \arccos E_2(x,y)]/2 - \pi. \\ \theta_S = [\varphi_1(x,y) - \varphi_2(x,y) + \arccos E_2(x,y) - \arccos E_1(x,y)]/4 \end{cases} \tag{4}$$

Referring to the meta-atoms for implementing $J_M(x,y)$ and $J_S(x,y)$, a series of subwavelength silicon pillars is designed to provide $\delta_{M,x}$, $\delta_{M,y}$, and θ_M, and another series of silicon pillars is selected to satisfy $\delta_{S,x}$, $\delta_{S,y}$, and θ_S. Figure 2(a) exhibits the schematic diagram and optical microscope image of the first demo sample—Metasurface I. All the silicon pillars are constructed on silicon substrate with square lattice constant

$P = 230$ μm and possess a uniform height (H) of 300 μm. The building block, named meta-molecules, contains two silicon pillars arranged at the main diagonal (silicon pillars M) and two silicon pillars arranged at the secondary diagonal (silicon pillars S) on a 2×2 square grid. The dimensions $D_{M,x}$, $D_{M,y}$ of silicon pillar M and $D_{S,x}$, $D_{S,y}$ of silicon pillar S specify the propagation phase shift, and their orientation angles θ_M and θ_S ascertain the geometry phase. In order to find appropriate silicon pillars that not only satisfy Eqs. (3) and (4) but also cover the phase range from 0 to 2π, we perform simulation using commercially available software computer simulation technology (CST) Microwave Studio. By sweeping the transmitted phase and amplitude with varied D_x and D_y, 24 silicon pillars with phase gradient $\pi/12$ are obtained at 0.6 THz. As one can observe in Fig. 2(b), the phase difference between δx and δy in the selected unit structures is π, and the phase shift (δx and δy) increases linearly by $\pi/12$ from 0 to 2π, which matches well with Eqs. (3) and (4). Additionally, the polarization conversion efficiency of selected silicon pillars is also validated to be higher than 80% as illustrated in Fig. 2(c).

With the 24 selected pillars, the design flow of the metasurface is depicted in Figs. 3(a)–3(d). For the first demo metasurface, the phase profiles of four POVs with TCs of 1, –1, 2, and –2 are calculated, respectively, as shown in Fig. 3(a). Subsequently, the POVs with TCs of 1 and –1 are superposed as the encoded information for RCP output while the superposition of POVs with TCs of 2 and –2 is given to the LCP output. The summarized amplitude and phase profiles consist of the target complex-amplitude distributions $E_1(x,y) \exp[i\varphi_1(x,y)]$ and $E_2(x,y) \exp[i\varphi_2(x,y)]$ as depicted in Fig. 3(b). In order to accomplish this manipulation through the metasurface, appropriate silicon pillars in every local pixel are selected and properly rotated to best meet the requirements given by Eqs. (3) and (4) [Fig. 3(c)]. After the combination between silicon pillar M and silicon pillar S, the final structure as shown in the middle of Fig. 3(d) is simulated in CST and the vortex purities under different incidences are calculated based
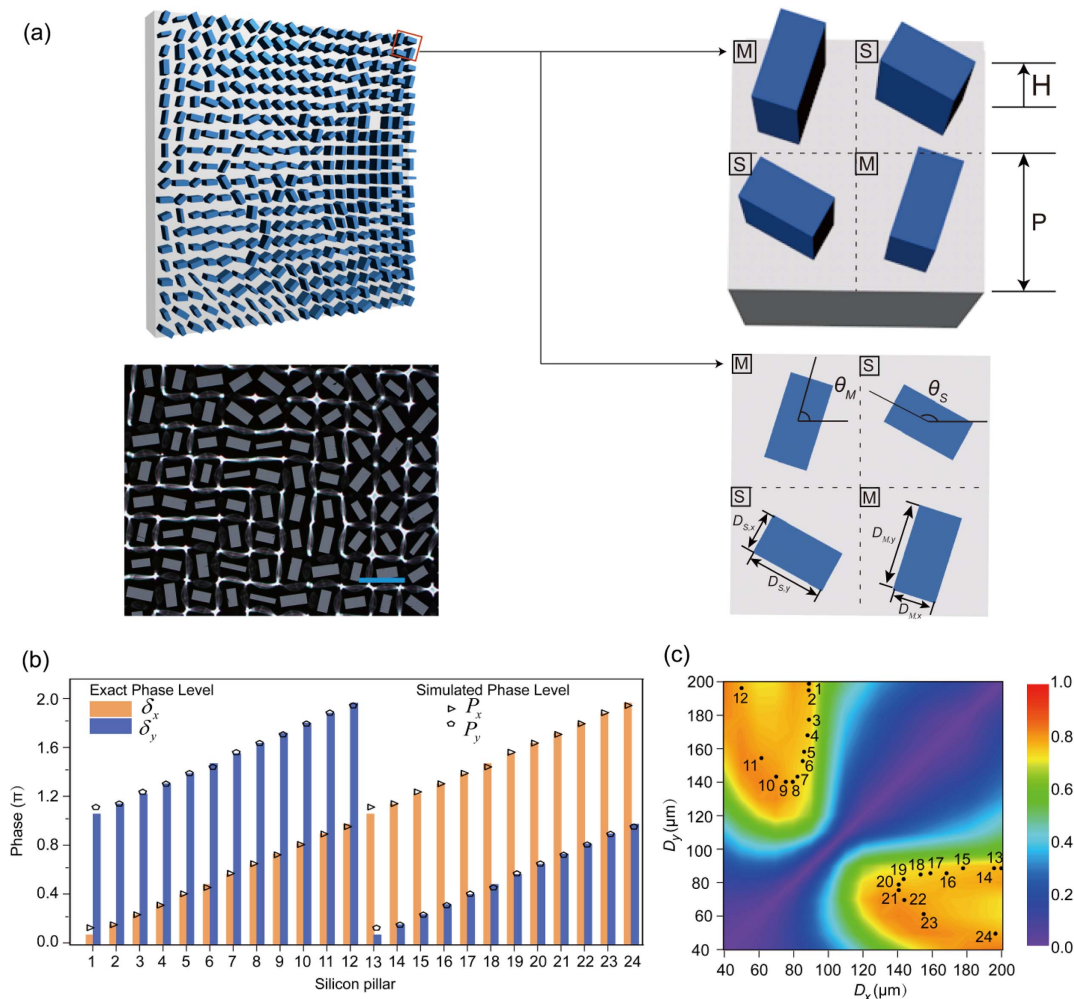
Fig. 2. Design of the meta-molecules of the metasurface. (a) Left, schematic diagram and optical microscope image of Metasurface-I made up of silicon pillars. Scale bar, 300 μm. Right, a typical meta-molecule including two diagonal silicon pillars M and two anti-diagonal silicon pillars S. (b) Twenty-four levels of discrete phase in the full range $[0, 2\pi]$ for exact phase level δ_x and δ_y (described by blue and yellow bars, respectively) and simulated phase level P_x and P_y (described by triangles and pentagons symbols, respectively). Each selected silicon pillar is an effective half-wave plate. (c) Calculated polarization conversion efficiency at 0.6 THz for varied dimensions (D_x and D_y) ranging from 40 μm to 200 μm. The selected silicon pillars are indicated as black dots.

on the simulated results. As displayed in Fig. 3(d), the designed metasurface shows perfect vortex purity that matches well with the setting TCs.

B. Independent Generation of Superposed POVs for LCP and RCP Incidences

The sample of Metasurface-I has an area of 23 mm × 23 mm composed of 100 × 100 silicon pillars. The fabrication of the sample and the measurement details can be found in Appendices A–C. Figures 4(a) and 4(d) illustrate the generated superposed POVs by the Metasurface-I sample under RCP and LCP incidence, respectively. Referring to the design parameters of POVs in Table 1, all POVs have an identical radius but different TCs. Figure 4(b) displays the calculated and measured focal profiles of the POVs' phase and intensity for LCP and RCP inputs at 0.6 THz. It is worth noticing that the intensity distributions are segmented into lobes, where the number of lobes is twice of $(l_a - l_b)/2$ [40,41]. For LCP incidence

[Fig. 4(b)], there are obviously two lobes, which is in line with the calculation $(l_{a1} - l_{b1})$. The phase profile also reflects the same tendency, which is divided into two discontinuous parts. Furthermore, the vortex purity calculated by the measured results is shown in Fig. 4(c), in which the mode weights with TC = 1 and −1 are remarkably higher than others. As for RCP incidence, the corresponding phase and intensity profiles of the Metasurface-I sample are shown in Fig. 4(e). Now the TCs of two generated LCP POVs are changed to 2 and −2, leading to the output intensity profiles with four lobes and the phase profiles with four discontinuous parts. Figure 4(f) further proves that the mode weights of preset TCs of 2 and −2 are distinctly higher than others. From Figs. 4(b) and 4(e), it is clear that the radii of intensity profiles are nearly the same for TCs of 1, −1, 2, and −2. The calculation of superposed POV radii is to examine this independence, and the radius of the intensity profile is defined as the rings formed by the inner circle (r_0) and the outer circle (r) as marked by the dashed
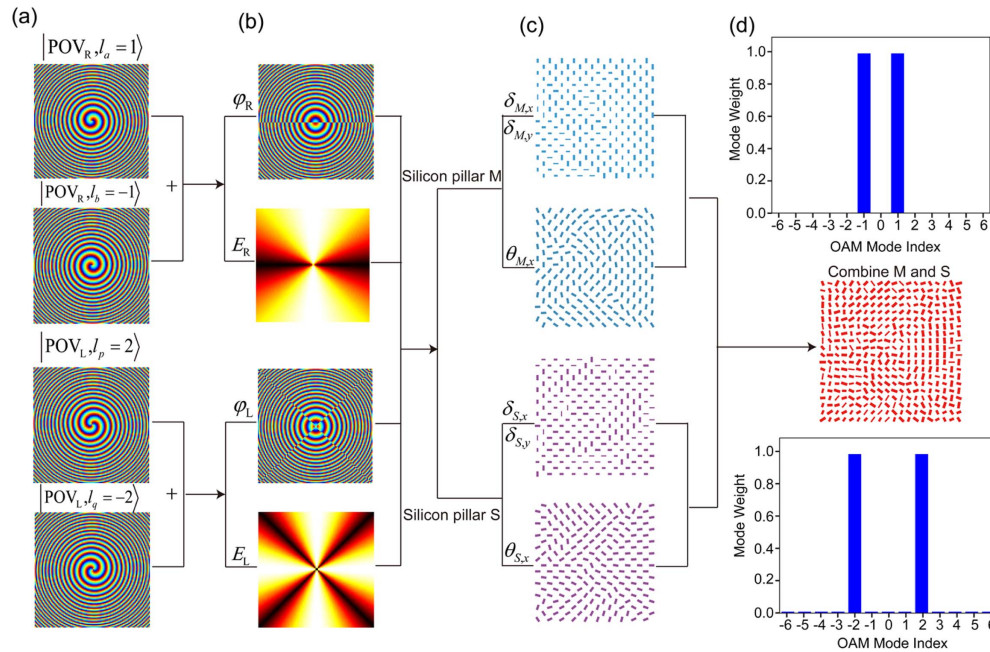
Fig. 3. Design flow of the metasurfaces. (a) Phase profiles of four POVs with TCs of 1, –1, 2, and –2 from top to bottom. (b) Target amplitude and phase profiles of superposed POVs, which are encoded on the metasurface. (c) Silicon pillars M and S, which depend on the setting parameters $(\delta_{M,x}, \delta_{M,y}, \delta_{S,x}, \delta_{S,y}, \theta_M, \text{ and } \theta_S)$. (d) Top, vortex mode purity of the superposition of $|\text{POV}_R, l_a = 1\rangle$ and $|\text{POV}_R, l_b = -1\rangle$. Middle, arrangement of the silicon pillars on the designed metasurface. Bottom, vortex mode purity of the superposition of $|\text{POV}_L, l_p = 2\rangle$ and $|\text{POV}_L, l_q = -2\rangle$.
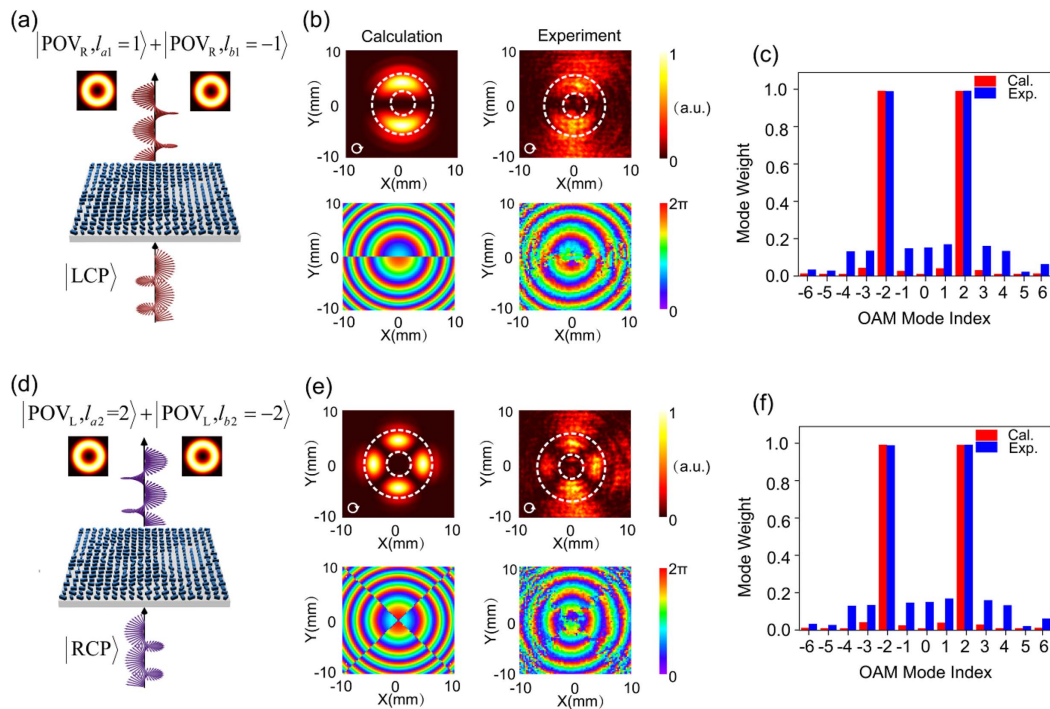
Fig. 4. Theoretical and experimental demonstration of Metasurface-I generating superposed POVs with different TCs and having an identical ring radius for LCP and RCP incidences. (a) Schematic diagram under LCP incidence. (b) Calculated and measured intensity and phase distributions under LCP incidence at 0.6 THz. The outer and inner radii of the ring pattern are r and r_0, respectively. (c) Calculated and measured purity of OAM modes for LCP incidence. The sampling radius in corresponding intensity profiles is 4.0 mm. (d) Schematic diagram under RCP input. (e) Calculated and measured intensity and phase distribution under RCP input states at 0.6 THz. (f) Calculated and measured purity of the OAM mode for RCP incidence. The sampling radius in the corresponding intensity profile is 4.6 mm.

**Table 1. Setting Parameters of Superposed POVs Provided by Metasurface-I and Metasuface-II[a]**

Metasurface	Input Polarization	POV Index	d (mm)	l	f (mm)	λ (μm)
I	LCP	a_1	2.5	1	14	500
	LCP	b_1	2.5	−1	14	500
	RCP	a_2	2.5	2	14	500
	RCP	b_2	2.5	−2	14	500
II	LCP	p_1	3.0	2	14	500
	LCP	q_1	2.5	−1	14	500
	RCP	p_2	3.0	1	14	500
	RCP	q_2	2.5	−3	14	500

[a] d, l, λ, and f indicate axicon period, topological charge, operating wavelength, and focal length, respectively.

circles in Figs. 4(b) and 4(e), in which the radii of the inner circle (r_0) can be inferred by the single POV radius approximated as $r_0 = \lambda f / d$ [42]. The measured results prove that r and r_0 of the RCP POV output are 5.3 mm and 2.4 mm, respectively, tremendously close to those of the LCP POV output ($r = 5.5$ mm and $r_0 = 2.5$ mm), which substantiates that Metasurface-I can generate superposed POVs with radii independent of TCs. The calculated intensity profiles show the analogous conclusions as r and r_0 are 6 mm and 2.3 mm, respectively, for input states with orthogonal circular polarization. Meanwhile, the inner circle rings (r_0) of the superposed POVs

are extremely close to the single POV calculated by the above formula ($r_0 = 2.8$ mm). Besides, we also evaluate the response independence of Metasurface-I from 0.5 to 0.7 THz (Appendix F, Fig. 9). We found that the lobe numbers are consistent with the calculated results, but the contour of lobes becomes more ambiguous as the frequency moves away from 0.6 THz, which is caused by the limited polarization conversion efficiency of the selected silicon pillars (Appendix F, Fig. 8).

In addition to the spin-multiplexed and equal-radius POV generation and superposition demonstrated by Metasurface-I, our design scheme of Metasurface-II with the same size as Metasurface-I can generate superposed POVs with different radii for LCP and RCP incidence [Figs. 5(a) and 5(b)], enabling novel vortex beam-based complex structured light, such as the radial twisted beam. Different from the conventional TC-dependent radial twist, the radial twist generated by Metasurface-II is TC-independent and spin-multiplexed, which has potential application in high-resolution refractive index sensing and optical tweezers [43,44]. From the design parameters of POVs in Table 1, the TCs and radii of two superposed POVs for LCP or RCP incidence are different while the radii of POVs in the two sets of superpositions for opposite circular polarization are correspondingly equal. The intensity and phase profiles of Metasurface-II at 0.6 THz are subsequently characterized computationally and experimentally,
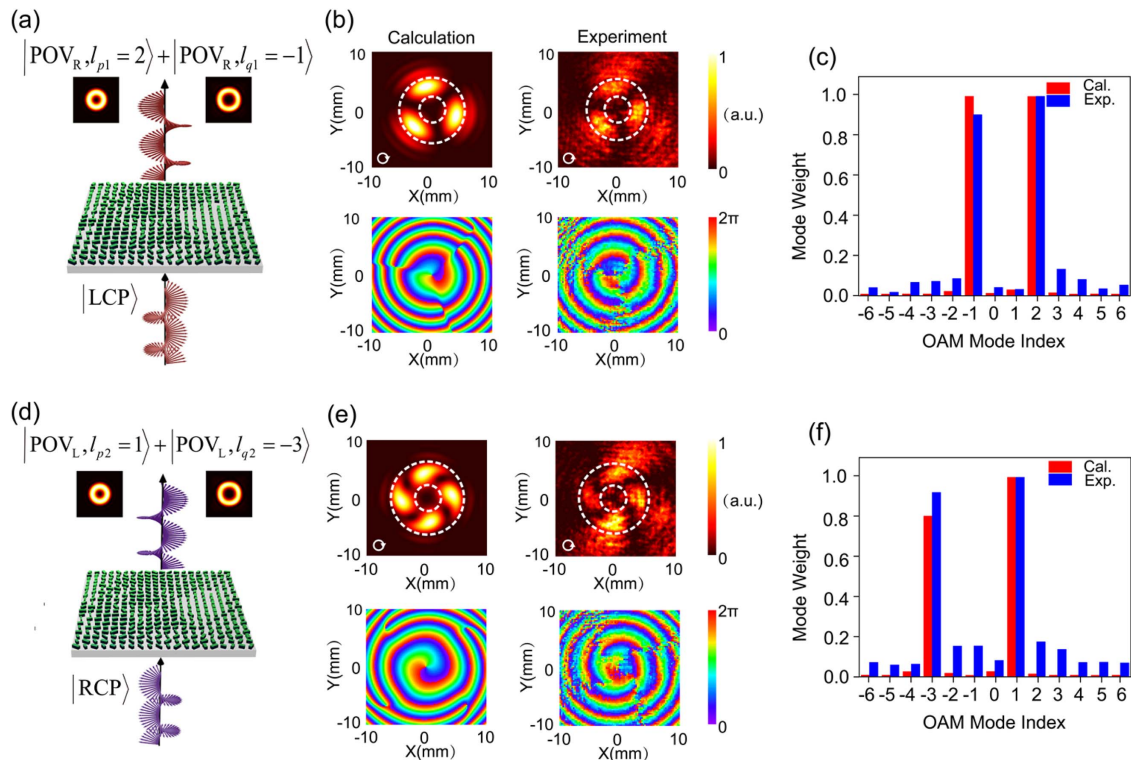
Fig. 5. Theoretical and experimental demonstration of Metasurface-II transforming LCP and RCP incidence into the superposition of two POVs with completely different TCs and radii. (a) Schematic diagram under LCP incidence. (b) Calculated and measured intensity and phase distributions under LCP incidence at 0.6 THz. The outer and inner radii of the ring pattern are r and r_0, respectively. (c) Calculated and measured purity of OAM mode for LCP incidence. The sampling radius in corresponding intensity profile is 3.7 mm. (d) Schematic diagram under RCP incidence. (e) Calculated and measured intensity and phase distributions under RCP incidence at 0.6 THz. (f) Calculated and measured purity of OAM mode for RCP incidence. The sampling radius in corresponding intensity profile is 3.7 mm.

as displayed in Figs. 5(b) and 5(e). The lobe numbers of the intensity distributions, under LCP and RCP incidences, are in accord with the calculation (L, $l_{p1} - l_{q1}$; R, $l_{p2} - l_{q2}$), and the numbers of discontinuities in the phase profiles are also identical to the lobe numbers. Besides, the vortex purity retrieved from the calculation and measurement is illustrated in Figs. 5(c) and 5(f). It is demonstrated that the mode weight of the scheduled TCs of –1 and 2 for LCP incidence remarkably exceed others. As for RCP incidence, the OAM modes of –3 and 1 are much higher than others as designed. We further compared the radii of the surrounding lobes under LCP and RCP incidences. The intensity profiles substantiate that the resulting lobes for both incidences will have nearly equal radius as long as the scheduled d for different incident polarizations are correspondingly equal. Here, the measured radii are 5.55 mm (r) and 2.50 mm (r_0), which only slightly deviate from the radii of calculated intensity ($r = 5.95$ mm, $r_0 = 2.32$ mm). Meanwhile, the inner circle rings (r_0) of the superposed POVs are approximately between the theoretical radii of two POVs ($r_0 = 2.3$ mm, $r_0 = 2.8$ mm) with the different radii. Moreover, the response independence of Metasurface-II from 0.5 to 0.7 THz is also evaluated (Appendix F, Fig. 10), and the results of Metasurface-II are similar to those of Metasurface-I.

3. CONCLUSION

In summary, we have proposed and demonstrated a spin-multiplexed all-dielectric metasurface to generate superposed terahertz POVs independently and simultaneously for LCP and RCP incidences. This adjustment endows input LCP and RCP states with tailored complex amplitudes of superposed POVs through changing the dimension and rotation angle of silicon pillars of every meta-molecule in the metasurface platform. As a proof-of-concept demonstration, Metasurface-I and Metasurface-II were designed, fabricated, and characterized to verify this sophisticated transformation. Not only the measured intensity and phase distributions but also the experimental purity of the vortex modes are consistent with the theoretical results, which confirm the function of the metasurfaces. This work paves a novel path toward investigating the photonic spin-Hall effect and developing an ultracompact and terahertz functional device for terahertz communication and complex structured generation.

APPENDIX A: NUMERICAL SIMULATIONS

The simulation in Fig. 2 was performed by leveraging the finite integration time domain solver of the computer simulation technology (CST) Microwave Studio software. In this simulation, we adopted periodic boundary conditions along both x and y directions in the rectangular silicon pillars. The refractive index of silicon pillars and the substrate is 3.45. The calculation of intensity and phase distributions of superposed POVs at the focal length f uses the Rayleigh–Sommerfeld diffraction integral,

$$U(x, y, z) = \frac{1}{i\lambda} \iint_s U(x_0, y_0)K(\theta)\frac{e^{ikr}}{r}\,\mathrm{d}s, \quad \textbf{(A1)}$$

where λ corresponds to the wavelength, and $U(x_0, y_0)$ represents the complex amplitude distribution of superposed

POVs at $z = 0$ with surface area s. r is the distance between the point in plane with $z = 0$ and the point in plane with $z = f$. $K(\theta)$ is the direction factor, defined as f/λ. $k = 2\pi/\lambda$ is the wavenumber.

The vortex purity is calculated based on the principle that the vortex beams with different TCs are orthogonal to each other. The definition of the mode weight is on the basis of the following calculation. First, a sampling ring that connects all the lobes in the intensity profile is selected. Subsequently, we calculate the integral value of the product of complex amplitude and $\exp(il\theta)$ over the sampling ring, which corresponds to the mode weight of TC l. As the modes of the optical vortex are numerous and complex, we only select the l from –6 to 6, which covers the TCs of superposed POVs. Finally, the extracted mode weights from calculations and experiments are normalized, respectively, to the maximum of the calculated and experimental values.

APPENDIX B: SAMPLE FABRICATION

The all-dielectric metasurface is fabricated by standard photolithography and deep reactive ion etching technology. The fabrication flow is shown in Fig. 6. First, a chromium layer of ≈10 nm thickness is sputtered on the high-resistivity double-side-polished silicon wafer (4 in. in diameter, 1 mm thick). Then, a layer of 10-μm-thick AZ2070 photoresist is spin-coated on this wafer. Subsequently, as the size of the fabrication is in the order of micron, the photoresist can be precisely patterned and developed by conventional UV photolithography with a photo mask custom-made by a company, and this procedure contains photoresist baking, alignment and exposure based on the mask, and photoresist development with a developer solution. After that, the chromium areas that were not protected by the photoresist were removed by acid eroding. Next, deep reactive ion etching was utilized to etch the undesired silicon areas to depth of 300 μm (frontside, sample layer) and 60 μm (backside, antireflection layer), and the
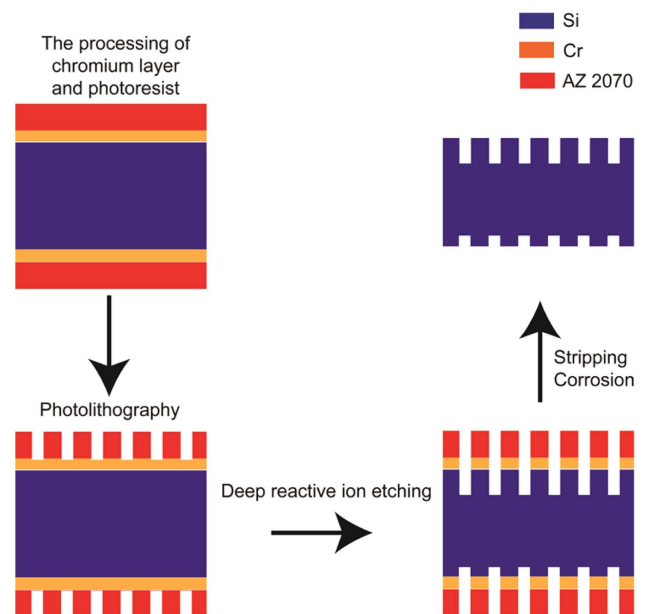

Fig. 6. Sample processing flow.

remaining photoresist and chromium served as a hard mask. Here, deep reactive ion etching is a process of a protecting and etching cycle. The etching and passivation gas are SF_6 and C_4F_8, respectively, and the etching power is between 50 and 3000 W. After a reaction-stripping-emission cycle of 6 s (etching, 4 s; passivating, 2 s), a certain vertical depth can be etched, and the final number of cycles can be determined according to the target depth. Finally, by separately cleaning the residual photoresist and chromium with acetone and acid, the dielectric metasurfaces were completed. In our etching process, the depth of etching is 300 μm ± 10 μm (frontside, sample layer) and 60 μm ± 3 μm, respectively, and the transverse dimension error is ±5%.

APPENDIX C: EXPERIMENTAL CHARACTERIZATION

The performance of the fabricated metasurface is measured by a homemade fiber-based near-field scanning terahertz time-domain spectroscopy system (Fig. 7). A photoconductive antenna is utilized as the transmitter, and the terahertz detector is a photoconductive probe with ≤ 20 μm resolution, which is placed at a 2D motorized translation stage to control the position of the detector. In the measured procedure, the emitted terahertz pulses with x polarization are first collected and collimated by a terahertz lens with a focal length of 50 mm. After passing through a terahertz linear polarizer (P1), the terahertz wave illuminates the fabricated metasurface from its backside. The output terahertz field transmitted another linear polarizer (P2), which is utilized to extract the target polarization components of the output beam. Finally, the output from the second linear polarizer is detected by the probe locating 14 mm above the metasurface. The experimental intensity and phase distributions displayed in Figs. 4 and 5 are scanned by 2D motorized translation stage with a moving range from −10 mm to 10 mm and an interval of 0.2 mm.
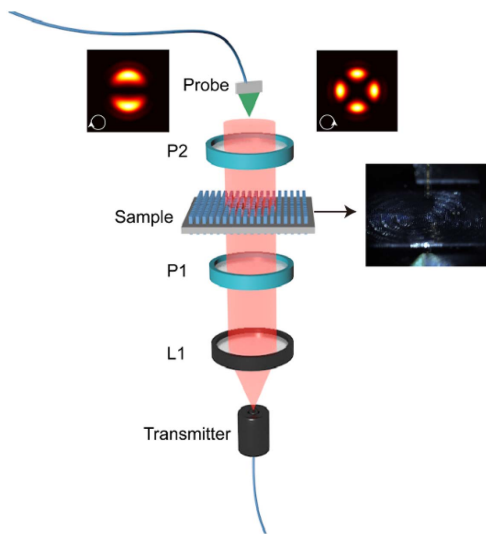
Fig. 7. Schematic of the near-field scanning terahertz time-domain spectroscopy system. Transmitter, terahertz photoconductive antenna; L1, terahertz lens; P1, terahertz linear polarizer 1; P2, terahertz linear polarizer 2; probe, terahertz near-field probe with ≥ 20 μm resolution.

In order to measure the response of the metasurfaces under LCP and RCP incidences, normally incident 45° and −45° polarized terahertz waves are first achieved by rotating P1 to +45° and then to −45°. At each orientation of P1, P2 is rotated to 45° and −45°, respectively, so that the near-field probe is able to detect the +45°- and −45°-polarized transmissions. In this manner, the four transmission coefficients for linearly polarized waves are obtained, and those are T_{++} (input: +45°; output: +45°), T_{--} (input: −45°; output: −45°), T_{+-} (input: +45°; output: −45°), and T_{-+} (input: −45°; output: +45°). The transmission coefficients for orthogonal circular polarization incidence are thereafter calculated,

$$T_{LR} = (T_{++} + T_{--}) - i(T_{+-} - T_{-+}), \tag{C1}$$

$$T_{RL} = (T_{++} + T_{--}) + i(T_{+-} - T_{-+}), \tag{C2}$$

where T_{LR} represents the RCP transmitted component in response to the LCP incidence, while T_{RL} represents the LCP transmitted component in response to the RCP incidence. Here, RCP is defined as a clockwise rotation of the electric field vector.

APPENDIX D: DERIVATION OF THE REQUIRED PHASE SHIFTS AND ORIENTATION ANGLES OF TWO LINEAR BIREFRINGENT OPTICAL ELEMENTS BASED ON J_M AND J_S

The Jones matrix $J(x, y)$ is a non-unitary matrix and cannot be directly diagonalized, so we mathematically decompose $E_1 \exp[i\varphi_1(x, y)]$ and $E_2 \exp[i\varphi_2(x, y)]$ into

$$E_1(x,y)e^{i\varphi_1(x,y)} = \cos\left(\frac{\varphi_M^1 - \varphi_S^1}{2}\right)e^{i\left(\frac{\varphi_M^1 + \varphi_S^1}{2}\right)} = \frac{e^{i\varphi_M^1} + e^{i\varphi_S^1}}{2}, \tag{D1}$$

$$E_2(x,y)e^{i\varphi_2(x,y)} = \cos\left(\frac{\varphi_M^2 - \varphi_S^2}{2}\right)e^{i\left(\frac{\varphi_M^2 + \varphi_S^2}{2}\right)} = \frac{e^{i\varphi_M^2} + e^{i\varphi_S^2}}{2}. \tag{D2}$$

By substituting Eqs. (D1) and (D2) into $J(x, y)$, we can transform $J(x, y)$ to

$$J(x,y) = \frac{J_M(x,y) + J_S(x,y)}{2}, \tag{D3}$$

$$J_M(x,y) = R_M \Lambda_M R_M^{-1} = [E_1 \quad E_2]\begin{pmatrix} \lambda_1 & 0 \\ 0 & \lambda_2 \end{pmatrix}[E_1 \quad E_2]^{-1}$$

$$= \begin{pmatrix} \cos\left(\frac{e^{i\varphi_M^1} - e^{i\varphi_M^2}}{4}\right) & \sin\left(\frac{e^{i\varphi_M^1} - e^{i\varphi_M^2}}{4}\right) \\ -\sin\left(\frac{e^{i\varphi_M^1} - e^{i\varphi_M^2}}{4}\right) & \cos\left(\frac{e^{i\varphi_M^1} - e^{i\varphi_M^2}}{4}\right) \end{pmatrix}$$

$$\times \begin{pmatrix} e^{i(\varphi_M^1 + \varphi_M^2)/2} & 0 \\ 0 & e^{i(\varphi_M^1 + \varphi_M^2)/2 - i\pi} \end{pmatrix}$$

$$\times \begin{pmatrix} \cos\left(\frac{e^{i\varphi_M^1} - e^{i\varphi_M^2}}{4}\right) & \sin\left(\frac{e^{i\varphi_M^1} - e^{i\varphi_M^2}}{4}\right) \\ -\sin\left(\frac{e^{i\varphi_M^1} - e^{i\varphi_M^2}}{4}\right) & \cos\left(\frac{e^{i\varphi_M^1} - e^{i\varphi_M^2}}{4}\right) \end{pmatrix}^{-1}, \tag{D4}$$

$$J_S(x,y) = R_S \Lambda_S R_S^{-1} = \begin{bmatrix} E_3 & E_4 \end{bmatrix} \begin{pmatrix} \lambda_3 & 0 \\ 0 & \lambda_4 \end{pmatrix} \begin{bmatrix} E_3 & E_4 \end{bmatrix}^{-1}$$

$$= \begin{pmatrix} \cos\left(\frac{e^{i\varphi_S^1} - e^{i\varphi_S^2}}{4}\right) & \sin\left(\frac{e^{i\varphi_S^1} - e^{i\varphi_S^2}}{4}\right) \\ -\sin\left(\frac{e^{i\varphi_S^1} - e^{i\varphi_S^2}}{4}\right) & \cos\left(\frac{e^{i\varphi_S^1} - e^{i\varphi_S^2}}{4}\right) \end{pmatrix}$$

$$\times \begin{pmatrix} e^{i(\varphi_S^1 + \varphi_S^2)/2} & 0 \\ 0 & e^{i(\varphi_S^1 + \varphi_S^2)/2 - i\pi} \end{pmatrix}$$

$$\times \begin{pmatrix} \cos\left(\frac{e^{i\varphi_S^1} - e^{i\varphi_S^2}}{4}\right) & \sin\left(\frac{e^{i\varphi_S^1} - e^{i\varphi_S^2}}{4}\right) \\ -\sin\left(\frac{e^{i\varphi_S^1} - e^{i\varphi_S^2}}{4}\right) & \cos\left(\frac{e^{i\varphi_S^1} - e^{i\varphi_S^2}}{4}\right) \end{pmatrix}^{-1}. \tag{D5}$$

It can be observed that the Jones matrices $J_M(x,y)$ and $J_S(x,y)$ can be satisfied using silicon pillars with the function of a half-wave plate. The phase shifts corresponding to the x- and y-polarized incidences and the rotation angle of the rectangular pillar are calculated in Eqs. (3) and (4).

APPENDIX E: CALCULATION OF POLARIZATION CONVERSION EFFICIENCY OF THE SILICON PILLAR

When an arbitrarily polarized light is incident on the single silicon pillars of metasurface, the resulting optical field distribution can be described as

$$|E_{\text{out}}\rangle = \eta_1 |E_{\text{in}}\rangle + \eta_R e^{i2\theta} |\text{RCP}\rangle + \eta_L e^{i2\theta} |\text{LCP}\rangle, \tag{E1}$$

where $\eta_1 = (T_x + T_y e^{i\varsigma})/2$, $\eta_R = [(T_x - T_y e^{i\varsigma})/2] \cdot \langle E_{\text{in}} | \text{LCP} \rangle$ and $\eta_L = [(T_x - T_y e^{i\varsigma})/2]\langle E_{\text{in}} | \text{RCP}\rangle$ are the transmission coefficients of output with various polarization and θ is the rotation angle of the fast axes of silicon pillars. In aforementioned three transmission coefficients, the T_x and T_y correspond to the transmission coefficients of the rectangular silicon pillars for the incident wavefront with the polarization direction parallel and perpendicular to the fast axis, and ς defines the phase difference between T_x and T_y. Thus, for LCP and RCP incidence, the polarization efficiency η_R^2 and η_L^2 of output state can be calculated as

$$\eta_R^2 = |[(T_x - T_y e^{i\varsigma})/2]\langle E_{\text{in}} | \text{LCP} \rangle|^2, \tag{E2}$$

$$\eta_L^2 = |[(T_x - T_y e^{i\varsigma})/2]\langle E_{\text{in}} | \text{RCP} \rangle|^2. \tag{E3}$$

APPENDIX F: BROADBAND RESPONSE OF FABRICATED METASURFACE-I AND METASURFACE-II FROM 0.5 THz TO 0.7 THz

In order to evaluate the broadband response of the proposed metasurface, we first analyze the performance of the selected 24 silicon pillars in the range of 0.5 THz to 0.7 THz. The simulation is carried out with the incident polarization parallel and perpendicular to the fast axis of the silicon pillars. For the sake of convenience, we arrange these two polarization directions as x polarization and y polarization. Figure 8 illustrates the calculated polarization conversion efficiency of the 24 silicon pillars in the range from 0.5 THz to 0.7 THz. Here the first 12 silicon pillars covering the phase range of π possess entirely
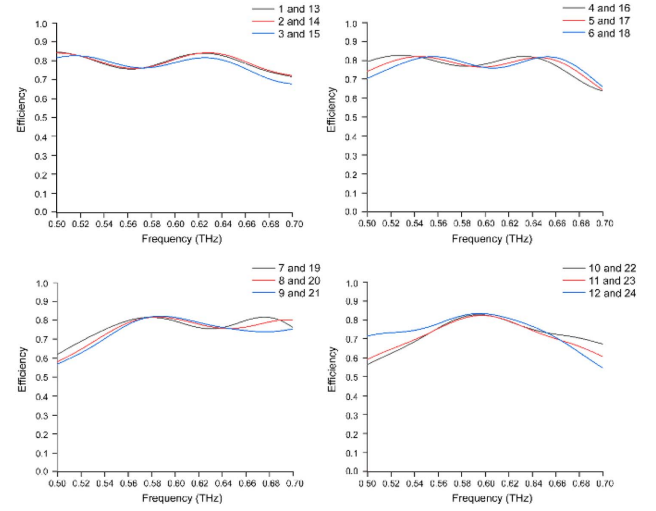

Fig. 8. Calculated polarization conversion efficiency of 24 silicon pillars in the range of 0.5 THz to 0.7 THz.

the same dimensions as the next 12 silicon pillars with exchanged x direction and y direction length. The results show that the polarization conversion efficiency of all silicon pillars is over 70% when the frequency is around the operating frequency 0.6 THz. The farther the frequency is away from 0.6 THz, the more the efficiency decreases. For example, the efficiency of 8, 9, 10, and 11 silicon pillars is lower than 60% at the frequency of 0.5 THz. These substantiate that the broadband response of the selected silicon pillars is limited. Besides, the intensity and phase distribution profiles of the fabricated Metasurface-I and Metasurface-II are also measured at the frequencies of 0.5 THz, 0.55 THz, 0.65 THz, and 0.7 THz as exhibited in Figs. 9 and 10. It can be clearly observed that the lobe numbers match well with the theoretical value but the
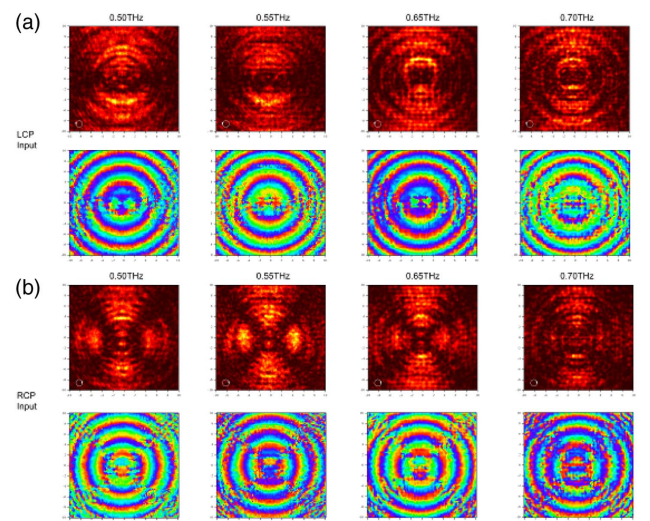
Fig. 9. Measured intensity and phase distribution corresponding to the output light from Metasurface-I at the frequencies of 0.50 THz, 0.55 THz, 0.65 THz, and 0.7 THz. (a) Experimental intensity and phase distribution for the incidence with LCP. (b) Experimental intensity and phase distribution for the incidence with RCP.

(a)

(b)
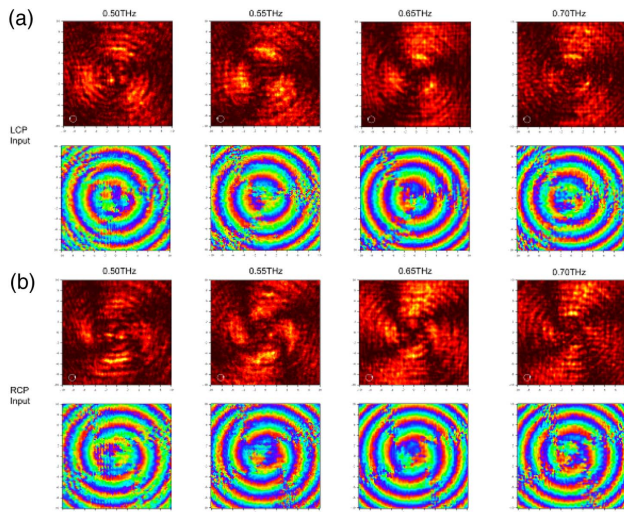
Fig. 10. Measured intensity and phase distribution corresponding to the output light from metasurface-II at the frequencies of 0.50 THz, 0.55 THz, 0.65 THz, and 0.7 THz. (a) Experimental intensity and phase distribution for the incidence with LCP. (b) Experimental intensity and phase distribution for the incidence with RCP.

contour of the lobes becomes more ambiguous as the frequency is further away from the anticipated 0.6 THz, which also proves that the metasurface is designed to achieve only a limited range of terahertz response.

APPENDIX G: DESIGN OF THE ANTIREFLECTION LAYER AND MEASUREMENT OF THE EFFICIENCY OF THE PROPOSED ALL-DIELECTRIC METASURFACE

On the purpose of improving the transmittance of the proposed metasurface, we also design a polarization-independent antireflection silicon pillar array at the other side of the silicon substrate to reduce reflectance at the operating frequency 0.6 THz, as indicated in Fig. 11. The unit structure is analogous to that in Fig. 2(a), but its lateral cross section is in a square shape with fixed side length $d_x = d_y = 42$ μm, height $h = 60$ μm, and periods $p_x = p_y = 52$ μm. To experimentally demonstrate the capacity of the antireflection layer, we physically arranged it at the back of metasurface and measured the integrated
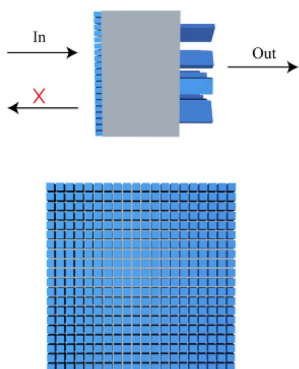
Fig. 11. Schematic of the dielectric antireflection silicon pillar array.

intensity of the output terahertz beams with ($I_S = cn_{air} \sum |E_S|^2 / 4\pi$) and without ($I_r = cn_{air} \sum |E_r|^2 / 4\pi$) the sample by the near-field terahertz time-domain spectroscopy system. For Metasurface-I, the measured efficiencies are 57.80% and 45.20% under LCP and RCP incidence. For Metasurface-II, the measured efficiencies are 48.22% and 42.3% under LCP and RCP incidence.

Disclosures. The authors declare no conflicts of interest.

Data Availability. Research data are not shared. The data that support the findings of this study are available from the corresponding author upon reasonable request.

Author Contributions. F. H. proposed the original idea, performed the theory, simulations, and experiments, and completed the first draft of the paper. Q. X. and J. G. conducted the theory and supervised the entire project. Q. X. proposed the theory. W. L. and T. W. helped with the experiment. W. Z., J. H., Q. X., and J. G. revised the paper. All the authors discussed the results.

REFERENCES

1. M. Born and E. Wolf, *Principles of Optics*, 6th ed. (Cambridge University, 1997).
2. R. A. Beth, "Mechanical detection and measurement of the angular momentum of light," Phys. Rev. **50**, 115–125 (1936).
3. L. Allen, M. W. Beijersbergen, R. Spreeuw, and J. J. Woerdman, "Orbital angular momentum of light and the transformation of Laguerre-Gaussian laser modes," Phys. Rev. A **45**, 8185–8189 (1992).
4. J. Leach, M. J. Padgett, S. M. Barnett, S. Franke-Arnold, and J. J. Courtial, "Measuring the orbital angular momentum of a single photon," Phys. Rev. Lett. **88**, 257901 (2002).
5. A. O'neil, I. MacVicar, L. Allen, and M. J. Padgett, "Intrinsic and extrinsic nature of the orbital angular momentum of a light beam," Phys. Rev. Lett. **88**, 053601 (2002).
6. S. M. Barnett and L. J. Allen, "Orbital angular momentum and nonparaxial light beams," Opt. Commun. **110**, 670–678 (1994).
7. G. Gibson, J. Courtial, M. J. Padgett, M. Vasnetsov, V. Pas'ko, S. M. Barnett, and S. J. O. Franke-Arnold, "Free-space information transfer using light beams carrying orbital angular momentum," Opt. Express **12**, 5448–5456 (2004).
8. J. Wang, J.-Y. Yang, I. M. Fazal, N. Ahmed, Y. Yan, H. Huang, Y. Ren, Y. Yue, S. Dolinar, and M. J. Tur, "Terabit free-space data transmission employing orbital angular momentum multiplexing," Nat. Photonics **6**, 488–496 (2012).
9. S. W. Hell and J. J. Wichmann, "Breaking the diffraction resolution limit by stimulated emission: stimulated-emission-depletion fluorescence microscopy," Opt. Lett. **19**, 780–782 (1994).
10. J. Leach, B. Jack, J. Romero, A. K. Jha, A. M. Yao, S. Franke-Arnold, D. G. Ireland, R. W. Boyd, S. M. Barnett, and M. J. Padgett, "Quantum correlations in optical angle–orbital angular momentum variables," Science **329**, 662–665 (2010).
11. M. P. MacDonald, L. Paterson, K. Volke-Sepulveda, J. Arlt, W. Sibbett, and K. J. Dholakia, "Creation and manipulation of three-dimensional optically trapped structures," Science **296**, 1101–1103 (2002).
12. V. Y. Bazhenov, M. Vasnetsov, and M. J. Soskin, "Laser beams with screw dislocations in their wavefronts," JETP Lett. **52**, 429–431 (1990).

13. M. Beijersbergen, R. Coerwinkel, M. Kristensen, and J. J. Woerdman, "Helical-wavefront laser beams produced with a spiral phaseplate," Opt. Commun. **112**, 321–327 (1994).

14. T. Wu, X. Zhang, Q. Xu, E. Plum, K. Chen, Y. Xu, Y. Lu, H. Zhang, Z. Zhang, and X. J. Chen, "Dielectric metasurfaces for complete control of phase, amplitude, and polarization," Adv. Opt. Mater. **10**, 2101223 (2022).

15. A. Zhan, S. Colburn, R. Trivedi, T. K. Fryett, C. M. Dodson, and A. J. Majumdar, "Low-contrast dielectric metasurface optics," ACS Photon. **3**, 209–214 (2016).

16. G. Zheng, H. Mühlenbernd, M. Kenney, G. Li, T. Zentgraf, and S. J. Zhang, "Metasurface holograms reaching 80% efficiency," Nat. Nanotechnol. **10**, 308–312 (2015).

17. A. H. Dorrah, N. A. Rubin, A. Zaidi, M. Tamagnone, and F. Capasso, "Metasurface optics for on-demand polarization transformations along the optical path," Nat. Photonics **15**, 287–296 (2021).

18. Q. Xu, X. Su, X. Zhang, L. Dong, L. Liu, Y. Shi, Q. Wang, M. Kang, A. Alù, and S. J. Zhang, "Mechanically reprogrammable Pancharatnam–Berry metasurface for microwaves," Adv. Photon. **4**, 016002 (2022).

19. D. Lin, P. Fan, E. Hasman, and M. L. Brongersma, "Dielectric gradient metasurface optical elements," Science **345**, 298–302 (2014).

20. S. Jahani and Z. J. N. Jacob, "All-dielectric metamaterials," Nat. Nanotechnol. **11**, 23–36 (2016).

21. M. Liu, W. Zhu, P. Huo, L. Feng, M. Song, C. Zhang, L. Chen, H. J. Lezec, Y. Lu, A. Agrawal, and T. Xu, "Multifunctional metasurfaces enabled by simultaneous and independent control of phase and amplitude for orthogonal polarization states," Light Sci. Appl. **10**, 107 (2021).

22. G. Biener, A. Niv, V. Kleiner, and E. J. Hasman, "Formation of helical beams by use of Pancharatnam–Berry phase optical elements," Opt. Lett. **27**, 1875–1877 (2002).

23. L. Marrucci, C. Manzo, and D. J. P. Paparo, "Optical spin-to-orbital angular momentum conversion in inhomogeneous anisotropic media," Phys. Rev. Lett. **96**, 163905 (2006).

24. S. Li, X. Li, L. Zhang, G. Wang, L. Zhang, M. Liu, C. Zeng, L. Wang, Q. Sun, and W. J. Zhao, "Efficient optical angular momentum manipulation for compact multiplexing and demultiplexing using a dielectric metasurface," Adv. Opt. Mater. **8**, 1901666 (2020).

25. Y. Xu, H. Zhang, Q. Li, X. Zhang, Q. Xu, W. Zhang, C. Hu, X. Zhang, J. Han, and W. J. N. Zhang, "Generation of terahertz vector beams using dielectric metasurfaces via spin-decoupled phase control," Nanophotonics **9**, 3393–3402 (2020).

26. R. C. Devlin, A. Ambrosio, N. A. Rubin, J. B. Mueller, and F. Capasso, "Arbitrary spin-to–orbital angular momentum conversion of light," Science **358**, 896–901 (2017).

27. J. Yu, C. Zhou, Y. Lu, J. Wu, L. Zhu, and W. J. Jia, "Square lattices of quasi-perfect optical vortices generated by two-dimensional encoding continuous-phase gratings," Opt. Lett. **40**, 2513–2516 (2015).

28. D. Deng, Y. Li, Y. Han, X. Su, J. Ye, J. Gao, Q. Sun, and S. J. Qu, "Perfect vortex in three-dimensional multifocal array," Opt. Express **24**, 28270–28278 (2016).

29. P. Vaity and L. J. Rusch, "Perfect vortex beam: Fourier transformation of a Bessel beam," Opt. Lett. **40**, 597–600 (2015).

30. Y. Liu, Y. Ke, J. Zhou, Y. Liu, H. Luo, S. Wen, and D. J. Fan, "Generation of perfect vortex and vector beams based on Pancharatnam-Berry phase elements," Sci. Rep. **7**, 44096 (2017).

31. J. García-García, C. Rickenstorff-Parrao, R. Ramos-García, V. Arrizón, and A. S. Ostrovsky, "Simple technique for generating the perfect optical vortex," Opt. Lett. **39**, 5305–5308 (2014).

32. A. S. Ostrovsky, C. Rickenstorff-Parrao, and V. Arrizón, "Generation of the 'perfect' optical vortex using a liquid-crystal spatial light modulator," Opt. Lett. **38**, 534–536 (2013).

33. W. Liu, Q. Yang, Q. Xu, X. Jiang, T. Wu, J. Gu, J. Han, and W. J. N. Zhang, "Multichannel terahertz quasi-perfect vortex beams generation enabled by multifunctional metasurfaces," Nanophotonics **11**, 3631–3640 (2022).

34. J. He, M. Wan, X. Zhang, S. Yuan, L. Zhang, and J. J. Wang, "Generating ultraviolet perfect vortex beams using a high-efficiency broadband dielectric metasurface," Opt. Express **30**, 4806–4816 (2022).

35. M. Liu, P. Huo, W. Zhu, C. Zhang, S. Zhang, M. Song, S. Zhang, Q. Zhou, L. Chen, H. J. Lezec, A. Agrawal, Y. Lu, and T. Xu, "Broadband generation of perfect Poincaré beams via dielectric spin-multiplexed metasurface," Nat. Commun. **12**, 2230 (2021).

36. Y. Zhang, W. Liu, J. Gao, and X. Yang, "Generating focused 3D perfect vortex beams by plasmonic metasurfaces," Adv. Opt. Mater **6**, 1701228 (2018).

37. Y. Bao, J. Ni, and C. W. Qiu, "A minimalist single-layer metasurface for arbitrary and full control of vector vortex beams," Adv. Mater. **32**, 1905659 (2020).

38. F. Aieta, P. Genevet, M. A. Kats, N. Yu, R. Blanchard, Z. Gaburro, and F. Capasso, "Aberration-free ultrathin flat lenses and axicons at telecom wavelengths based on plasmonic metasurfaces," Nano Lett. **12**, 4932–4936 (2012).

39. M. Khorasaninejad, W. T. Chen, R. C. Devlin, J. Oh, A. Y. Zhu, and F. Capasso, "Metalenses at visible wavelengths: diffraction-limited focusing and subwavelength resolution imaging," Science **352**, 1190–1194 (2016).

40. S. Franke-Arnold, J. Leach, M. J. Padgett, V. E. Lembessis, D. Ellinas, A. J. Wright, J. M. Girkin, P. Öhberg, and A. S. Arnold, "Optical Ferris wheel for ultracold atoms," Opt. Express **15**, 8619–8625 (2007).

41. L. Nie, L. Kong, T. Gao, N. Dong, and K. Jiang, "Characterizing the temporal rotation and radial twist of the interference pattern of vortex beams," Opt. Commun. **518**, 128339 (2022).

42. S. Fu, T. Wang, and C. Gao, "Perfect optical vortex array with controllable diffraction order and topological charge," J. Opt. Soc. Am. A **33**, 1836–1842 (2016).

43. A. H. Dorrah, M. Zamboni-Rached, and M. Mojahedi, "Experimental demonstration of tunable refractometer based on orbital angular momentum of longitudinally structured light," Light Sci. Appl. **7**, 40 (2018).

44. G. Liang, B. Yuan, B. Li, X. Kong, W. Cheng, H. Qiao, and X. Hu, "Evolutions of optical vortices under wide Gaussian background," Results Phys. **26**, 104352 (2021).